Plasma Chemistry and Plasma Processing, Vol. 3, No. 2, 1983

Plasma Polymerization of Ethane. I. Experimental Studies of Effluent Gas Composition and Polymer Deposition Rates

R. J. Jensen,[1,2] A. T. Bell,[1] and D. S. Soong[1]

Received October 8, 1982; revised February 8, 1983

The plasma polymerization of ethane was studied in a flow reactor of rectangular cross section. The plasma was sustained between parallel-plate electrodes by an RF generator operating at 13.56 MHz. The composition of the gas leaving the reactor was analyzed by gas chromatography. Polymer deposition rates were measured as a function of axial position in the reactor, using a quartz-crystal microbalance. The effluent gas is composed primarily of unreacted C_2H_6 and H_2. Significant concentrations of CH_4, C_2H_4, C_2H_2, and C_3H_8, and small amounts of C_3H_6, i-C_5H_{12}, and n-C_5H_{12}, are also observed. The distribution of these products is a strong function of the discharge power and of the gas pressure and residence time in the plasma. These experimental variables also affect both the rate of polymer deposition and the shape of the deposition profile along the reactor axis.

KEY WORDS: RF plasma; plasma polymerization; gas chromatrography; experimental.

1. INTRODUCTION

A large body of literature[1–8] has been devoted to the formation of polymer films in a low-pressure electric discharge, via the process known as plasma polymerization. This work has been motivated by the desire to produce new types of polymers suited for such purposes as reverse osmosis membranes,[9,10] permselective membranes,[11–14] thin-film capacitors,[15] passivating coatings for microelectronic devices,[16] waveguides for integrated optical circuits,[17] antireflective or moisture-resistant coatings for optical components,[18,19] and biocompatible coatings.[20,21] In contrast to conventional polymerization methods, plasma polymerization produces

[1] Department of Chemical Engineering, University of California, Berkeley, California 94720.
[2] Present address: Honeywell Corporate Technology Center, 10701 Lyndale Avenue S., Bloomington, Minnesota 55420.

0272-4324/83/0600-0139$03.00/0

an amorphous, network-like polymer that is highly crosslinked. Furthermore, the stoichiometry and functional group distribution of the polymer most often do not reflect those of the monomer. For example, plasma-polymerized ethylene contains both single and double bonds as well as aromatic groups[7] The H/C ratio of such polymers ranges between 1 and 2, and the crosslinked densities are on the order of one crosslink per 6 to 10 backbone atoms,[22] and the exact composition and structure of the polymer depends on the conditions of deposition.

The kinetics of film deposition have been studied for a variety of monomers and reactor configurations (e.g., Ref. 8). Most of this work, though, has been conducted in reactors which produce a poorly defined plasma volume, and one which often changes with reaction conditions. In all but a very few instances, only the overall polymer deposition rate was measured, and no attempt was made to determine the deposition rate profile and its dependence on plasma conditions. Compositional analysis of the gas effluent from the reactor has been carried out in only a limited number of cases.

The objective of this study was to obtain quantitative information about the kinetics of plasma film deposition and to gain a better understanding of the fundamental phenomena involved. Ethane was chosen as the monomer because it forms a film product over a wide range of reaction conditions, and because it yields relatively simple gas-phase products whose chemistry is well understood. In this paper we report the measurement of local deposition rates and effluent gas composition, measured over a range of operating conditions. A model of the deposition kinetics, based on a detailed consideration of the mass transport and elementary chemical reactions, will be presented separately.[23]

2. EXPERIMENTAL

2.1. Apparatus

The experimental apparatus consisted of three major parts: (1) a plasma reactor and associated gas-handling system, (2) a gas chromatograph, and (3) a quartz-crystal microbalance. A schematic of the complete apparatus is shown in Fig. 1.

The reactor consisted of a Lucite (polymethyl methacrylate) box into which were mounted a pair of hollow copper electrodes. A detailed drawing of a reactor is shown in Fig. 2. The electrodes were 15.3 cm wide by 20.3 cm long, and the gap between them was 4.4 cm. The rectangular-shaped reactor was enclosed in a 23-cm-diameter cylindrical Lucite shell. The application of large pressure differentials across the reactor was avoided by maintaining

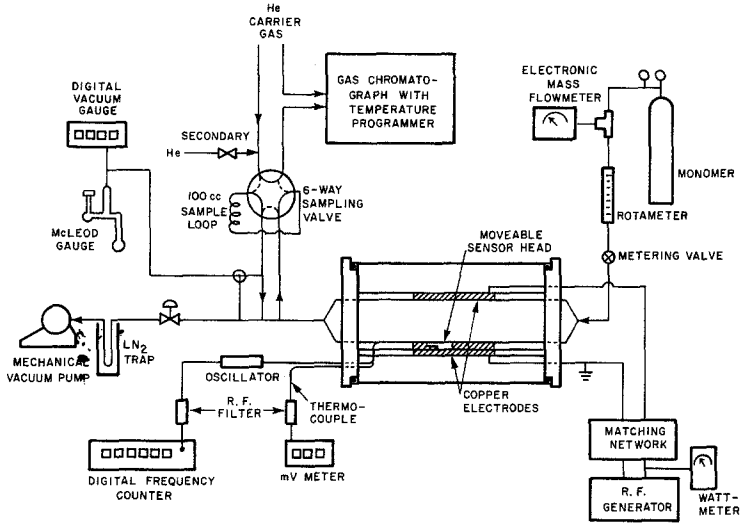

Fig. 1. Experimental apparatus.

the interior of the reactor and the space between the reactor and the shell at the same pressure. The reactor and surrounding shell were evacuated with a mechanical vacuum pump (Welch Model 1397). A liquid-nitrogen cold trap was installed between the pump and the reactor to protect the pump from condensible reaction products and to prevent the backstreaming of pump oil vapor. With no monomer flow, the reactor could be evacuated to 0.02 torr in 1–2 h. Tests carried out with a helium plasma failed to deposit polymer films on either electrode, indicating that the Lucite walls of the reactor do not release material that could form a polymer film.

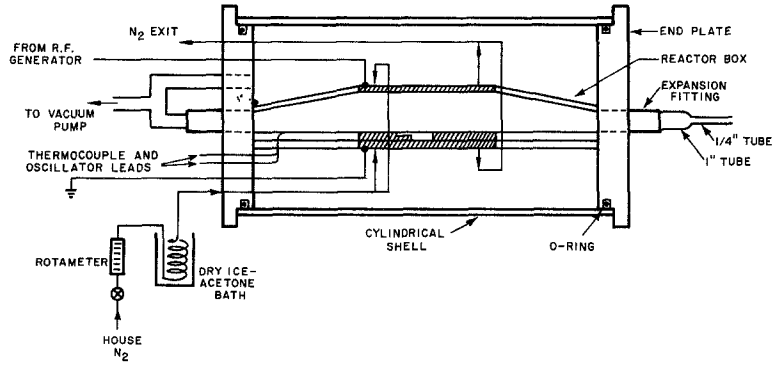

Fig. 2. Plasma reactor.

The monomer was Matheson CP grade ethane (99.9% minimum purity) and was used as supplied. Monomer flow rate was controlled with a micrometering valve. Flow rates of 0 to 20 STP cm^3/min were measured with an electronic mass flowmeter (Matheson Model 8110), and flow rates of 20 to 100 STP cm^3/min were measured with a glass-float rotameter (Matheson No. 610). The pressure upstream of the rotameter was controlled by a regulator and accurately measured with a Bourdon gauge.

Reactor pressures of 1–4 torr were controlled by balancing the vacuum pumping rate against the inlet flow rate. This was done by varying the cross section of a 3/4 in.-vacuum hose with a carpenter's jaw clamp. Pressure was measured at the exit end of the reactor with either a mercury-filled McLeod gauge or an electronic variable-capacitance vacuum gauge (MKS Tru-Torr).

Power to sustain the plasma was supplied by an RHF generator (International Plasma Corp., Model PM104 B), operating at a fixed frequency of 13.56 MHz with a maximum output of 150 W. The hot lead was connected to the upper electrode through an LC impedance matching network, and the lower electrode was grounded. Both the forward and reflected power could be measured with a wattmeter (Bird Model 40 Thru-line).

Both electrodes were cooled by circulating house nitrogen, cooled in a dry ice/acetone bath, through internal channels in the electrodes. Nitrogen flow rates of up to 1700 liters/h were required to keep the electrode temperature below about 85°C. It should be noted, though, that the temperature was dependent on operating conditions and could not be varied independently over a wide range by adjusting the flow rate of the cooling fluid.

A gas chromatograph (Loenco Model 240-T4) equipped with a thermal-conductivity detector was used to analyze the composition of the reactor effluent. The chromatograph was connected to the exit line of the reactor through a 6-way sampling valve (Whitey). During normal operation, with the valve in the position shown in Fig. 1, a side stream of reactor product flowed through a 100-cm^3 sample loop, while helium carrier gas was directed through bypass ports to the gas chromatograph column. When the sample valve was actuated, the carrier gas flushed the sample into the gas chromatograph, while the reactor product stream flowed through the bypass ports. A secondary source of helium was used to pressurize the sample loop up to the column head pressure of about 70 psig when the valve was switched. The pressure inside the sample loop could be measured prior to sampling with either the McLeod gauge or the electronic vacuum gauge, in order to accurately determine the total quantity of sample.

The chromatograph column was a 1/8-in. stainless steel tube, 20 ft long, packed with 100–200 mesh Durapak *n*-octane/Porasil C (Waters Associates). To achieve the desired separation on a single column, the column oven temperature was programmed from −50 to +65°C, at a rate of 14°C/min, beginning 1 min after sample injection. The initial temperature was achieved by placing a basket of dry ice in the column oven and allowing at least 15 min for equilibration.

Local deposition rates were measured with a quartz crystal microbalance. This device detects mass deposition onto an electrically excited quartz crystal by sensing the change in resonant frequency. The components comprising the microbalance are shown in Fig. 1. The transducer is a standard sensor obtained from Inficon Leybold–Heraeus, Inc., and consists of a holder containing a 6-MHz AT-cut quartz crystal with gold-plated electrodes. A small external oscillator and power supply are used to drive the crystal. The resonant frequency of the coupled oscillator and crystal was measured with a Data Precision Model 5740 Multifunction Counter. This instrument permitted frequencies to be measured with a precision of ±1 Hz. With this sensitivity thickness changes on the order of 10^{-8} g/cm^2 could readily be measured.

A low-pass RF filter was used between the oscillator signal cable and the frequency counter to eliminate the strong RF interference caused by the plasma. Without the filter it was impossible to obtain stable frequency readings with the plasma on. The temperature of the sensor head was measured with a copper/constantan thermocouple pressed into a small hole drilled in the sensor head. Output from the thermocouple was filtered by a low-pass filter and displayed on a Newport digital millivoltmeter to an accuracy of ±0.01 mV, equivalent to ±0.25°C.

To permit measurement of axial deposition profiles, the microbalance sensor was mounted in a copper plate, which could slide in a slot milled in the lower electrode. Details of this construction are shown in Fig. 3.

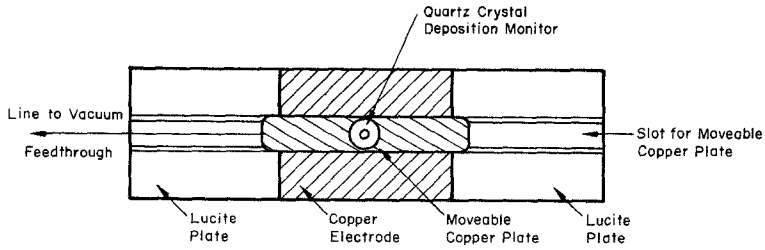

Fig. 3. Overhead view of the lower electrode plate with the moveable sensor.

The upper cover of the sensor was machined to bring the surface of the crystal as close as possible to the surface of the electrode. The surfaces of the sliding plate and the lower electrode were made flush to minimize perturbation of the plasma. The sliding plate, with the sensor inserted, was moved by pulling on a monofilament line which exited the reactor through a vacuum feedthrough.

The quartz microbalance was calibrated by weighing films deposited onto ferrotype plates and aluminum foil substrates placed around the sensor head. Calibration runs were done at 2 torr, 100 W, and 10, 20, 40, and 80 STP cm^3/min. An average of nine calibrations gave a value of $K = 4.30\ (\pm 0.50) \times 10^8$ Hz mg/cm^2. Considering the large uncertainty, this value was close enough to the theoretical value of $K = 4.417 \times 10^8$ Hz mg/cm^2 to justify use of the latter value in subsequent calculations.

The temperature coefficient, $\alpha_T = \partial f / \partial T$, was determined for each crystal by monitoring frequency changes while the electrodes were both heated and cooled from 0 to 70°C with the plasma off. Temperature coefficients were also measured as the electrodes cooled after a series of deposition experiments. The frequency versus temperature plots were linear over a wide range, and the values of α_T ranged from −4 to −17 Hz/°C for different crystals.

2.2. Procedure

Prior to initiating a new set of experiments, or after 5 to 10 h of operation, the reactor was disassembled and cleaned. Polymer film was dissolved off the electrodes and quartz crystals with trichloroethylene, and the Lucite surfaces were cleaned with xylene. After reassembly, the system was pumped down for at least an hour before starting any experiments.

To produce a plasma, the monomer flow rate was set first and then the reactor pressure was established by tightening the vacuum hose clamp. Sufficient time was allowed for the system to reach steady state. The flow of cooled nitrogen through the electrodes was usually started just before initiating the discharge. RF power was then turned on and the matching network was tuned to minimize reflected power. When the discharge came on, the reactor pressure usually increased rapidly by 10% to 100%, and was immediately readjusted to the desired operating value.

When the reactor effluent composition was to be analyzed, the gas chromatograph oven temperature was reduced to −50°C with dry ice prior to starting the plasma. Because the RF signal used to sustain the plasma interfered with the normal operation of the recorder and temperature programmer, these instruments were turned off while the plasma was on.

The plasma was allowed to run for at least 15 min before the effluent was sampled. Just before sampling, the sample loop pressure was measured, and the toggle valve to the secondary helium supply was opened. When the 6-way valve was switched, the sample was automatically pressurized and injected into the chromatograph column. Immediately after sampling, the plasma was turned off and the recorder and temperature programmer were turned on. After about 10 sec the toggle valve was closed, and after 1 min the temperature program was started. About 30 min were required to elute all of the products from the chromatograph column.

Deposition-rate measurements were begun as soon as the plasma conditions of pressure, power, and flow rate reached steady state. Frequency and thermocouple readings were taken at regular intervals, typically 30 to 120 sec. Longer time intervals were used when the deposition rate was lower, in order to equalize experimental uncertainty. The following calculations were used to determine deposition rates:

$$r_p = \frac{(4.417 \times 10^8)(1/f_2' - 1/f_1)}{\Delta t/3600} \tag{1}$$

$$f_2' = f_2 + \alpha_T(T_2 - T_1) \tag{2}$$

where r_p is the deposition rate in mg/cm^2 hr, f is the measured frequency in Hz, Δt is the time interval in sec, α_T is the temperature coefficient, T is the sensor temperature in °C, and subscripts 1 and 2 refer to initial and final readings, respectively. A Commodore PET computer was programmed to perform the above calculations and output the results on a thermal printer after each time interval.

The above calculations were repeated until no net drift in deposition rate was observed for at least 10 min, so that a number of measurements could be averaged. If a deposition rate profile was being measured, the sensor could be repositioned without interrupting the plasma operation. After measuring deposition rates at several different positions, the sensor was returned to its original position to check for a long-term drift in deposition rate. The electrode and sensor temperature usually increased slowly over long periods of time. If the temperature exceeded 80°C, the plasma was shut off and the electrodes were allowed to cool.

3. RESULTS AND DISCUSSION

3.1. Appearance of the Plasma

To obtain accurate and repeatable deposition rates, it was important to have the interelectrode region completely filled by a uniform plasma with sharp borders at the edges of the electrodes. These requirements were

met fairly well at 2 torr over the full range of flow rates, at powers above 50 W. At 1 torr, the plasma tended to spread outside the electrode boundaries, especially along the sliding plate. At pressures of 4 torr, and at 2 torr and powers below 50 W, the plasma usually filled only 1/2 to 3/4 of the interelectrode volume. Under these conditions the glow was very weak along the side walls of the reactor box, and the plasma formed an oval pattern, usally in the upstream portion of the interelectrode region. Occasionally this partial plasma would suddenly shift to a different position without changing its size. This shift could be induced by slight movements of the sliding plate or by repositioning the sensor.

3.2. Appearance of the Polymer Deposit

The main product deposited on the electrodes was a film, under all conditions for which a stable plasma could be maintained (i.e., 1–4 torr, 5–100 STP cm^3/min, and 50–175 W). The color of the films varied from pale yellow to dark gold. Thickness gradients frequently appeared as bands of color in very thin films. The initially deposited films usually adhered well to the metal surfaces and could be removed only by soaking in trichloroethylene and scrubbing. After long periods of deposition, the thick films became flaky and partially peeled away from the electrodes. Visible films were also deposited on the reactor side walls and on surfaces outside the electrode region. Slightly heavier film deposition seemed to occur on the upper (RF-active) electrode.

All of the experiments done at 1 torr and 100 W produced some powder in addition to film. At high flow rates, the powder was very fine, while at low flow rates it turned into large fluffy particles or filamentous strands after long periods of deposition. The thickest powder was usually deposited on the upper electrode, and sometimes powder appeared everywhere except on the sliding plate and crystal holder. Very little powder was formed at 2 torr, but the films were often cloudy, indicating the incorporation of small particles.

At 4 torr, a tacky film was formed, and occasionally a few oil droplets less than 1 mm in diameter were deposited. Often an oval ring of sticky film formed around the edges of a solid film, where the ring corresponded to the edges of the partial plasma.

3.3. Effluent Gas Composition

A typical chromatogram of the products from an ethane discharge is shown in Fig. 4. All of the labeled peaks were identified by comparing elution times with those for known components in a calibration gas mixture.

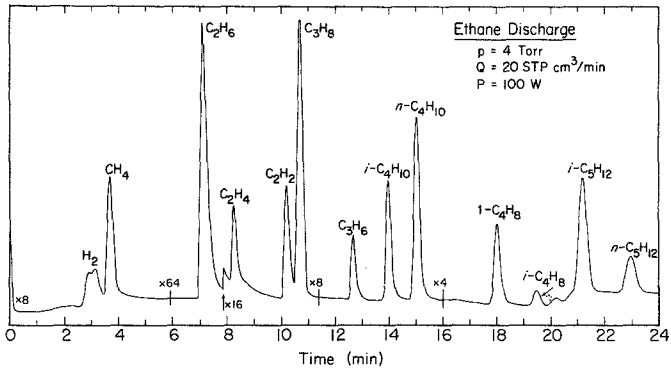

Fig. 4. Typical gas chromatogram of the reactor effluent.

The identities of the unlabeled peaks were identified by comparison of the observed elution times with published values for the same column packing.[24,25] The small peak between isobutene and isopentane probably represents *cis*- or *trans*-2-butene, but could also be 1,3-butadiene or propyne. The broad shoulder on the downstream side of the ethylene peak is probably due to trace amounts of water vapor. Several small, unidentified peaks often appeared beyond the *n*-pentane peak, indicating additional saturated and unsaturated C_5 and C_6 hydrocarbons.

The composition of the effluent gas provides an insight into the elementary reactions occurring in the plasma. The high concentration of H_2, coupled with significant mole fractions of C_2H_4 and C_2H_2, give strong evidence for hydrogen elimination reactions. The formation of unsaturated C_2 hydrocarbons is significant since these species are known to undergo rapid polymerization.[7,8] In view of this, C_2H_4 and C_2H_2 may be regarded as derivative monomers and very likely precursors to polymer formation. The presence of CH_4 indicates the dissociation of the monomer molecule into CH_3 or CH_2 fragments. The presence of single-carbon fragments is also consistent with the appearance of odd-carbon-numbered C_3 and C_5 hydrocarbons. Finally, the observation of C_3, C_4, and C_5 hydrocarbons indicates the occurrence of chain growth reactions in the gas phase.

The effect of reaction pressure on the effluent gas composition at a fixed flow rate and power is shown in Fig. 5. Most of the effluent gas is composed of C_2H_6 monomer and H_2, and these species have an opposite dependence on pressure. As the pressure is increased, more unconverted monomer appears in the effluent, and less H_2 is formed. This probably results from a decrease in both the electron energy and density with increasing pressure,[26] with concomitant reduction in the rate of monomer

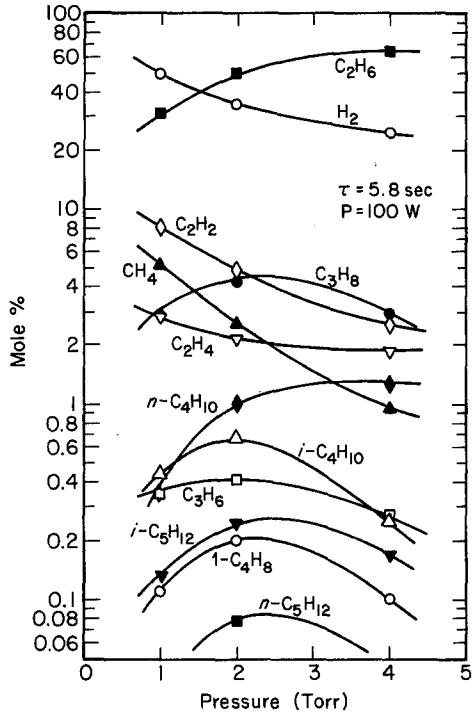

Fig. 5. Effect of pressure on the distribution of products in the reactor effluent.

dissociation and H_2 production by electron collisions. The mole fractions of the low-molecular-weight products, CH_4, C_2H_2, and C_2H_4, also decrease with increasing pressure. By contrast, the mole fractions of C_3, C_4, and C_5 hydrocarbons increase with increasing pressure up to pressures of 2–3 torr, and then decrease with further pressure increase. This indicates two competing effects. At low pressures, the high electron energies and densities promote the dissociation of gas-phase products to form low-molecular-weight species. As the pressure is increased, the electron energy and density decrease, and the reactant concentration increases, favoring chain growth to form higher-molecular-weight products. However, with further increase in pressure, the reduced conversion of monomer becomes a limiting factor, and production of high-molecular-weight products is reduced.

Figure 6 shows the effect of discharge power on effluent gas composition. Monomer consumption and H_2 production both increase with increasing power. The concentrations of all the derivative components initially increase with increasing power, due to the increased monomer conversion. However, at powers above 100 W, the concentrations of most of the C_3,

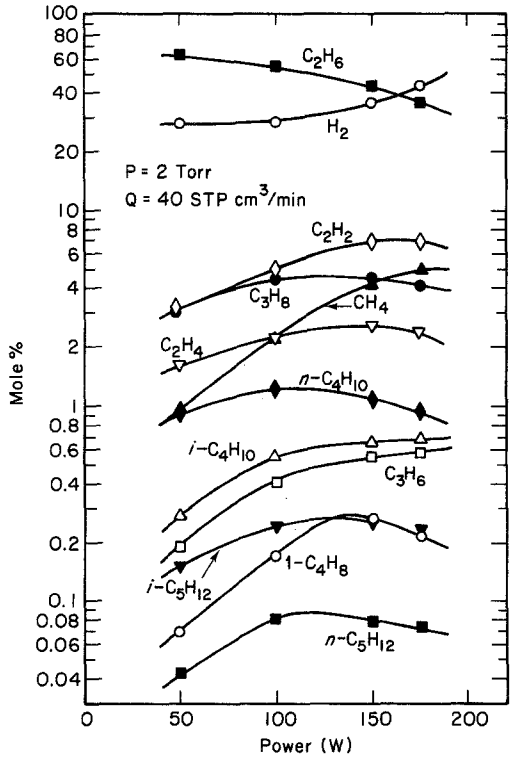

Fig. 6. Effect of power on the distribution of products in the reactor effluent.

C_4, and C_5 hydrocarbons decrease with increasing power, indicating the intensified dissociation of large molecules due to increased electron densities.[26] Straight-chain hydrocarbons, such as *n*-butane, are reduced to a greater extent at high power than the branched compounds such as isobutane. Increased power also favors the formation of unsaturated compounds; for example, propane decreases at high power while propylene increases, and ethylene falls off more rapidly than acetylene. The fraction of methane, the smallest stable hydrocarbon, steadily increases with increasing power.

The effect of monomer flow rate on effluent composition at fixed pressure and power is shown in Fig. 7. Monomer flow rate is inversely proportional to space time at a fixed pressure. As flow rate is decreased, the space time increases and thus the average residence time of the gas mixture in the plasma increases. The data in Fig. 7 shows that monomer consumption, and H_2 and CH_4 production, continually increase as the flow rate is decreased. The mole fractions of the other hydrocarbon products

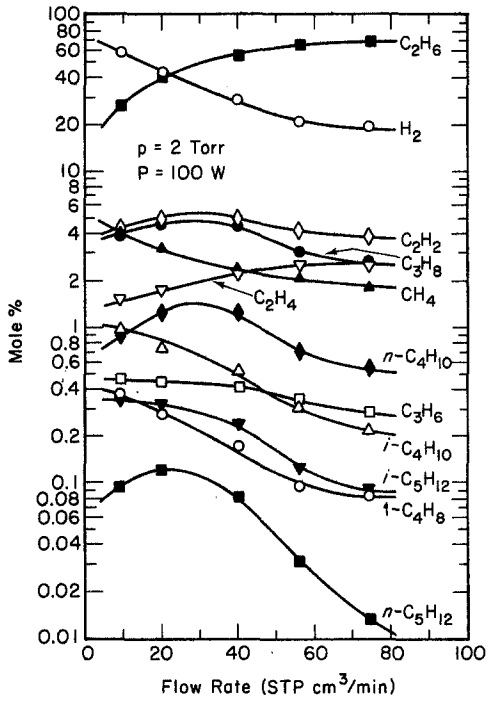

Fig. 7. Effect of monomer flow rate on the distribution of products in the reactor effluent.

initially increase with decreasing flow rate, due to increased monomer conversion. However, several of these components reach a maximum concentration and fall off with further decrease in flow rate. This may be due either to a loss of the reactant required to form the component, or an increased rate of consumption of the component.

The combined effects of flow rate and pressure can be seen more clearly by plotting gas composition as a function of space time. This characteristic, τ, is defined by

$$\tau = \frac{V_p(p/p_0)}{Q_0} \tag{3}$$

where V_p is the plasma volume, Q_0 is the monomer volumetric flow rate measured at STP, p is the reactor pressure, and p_0 is 760 torr. Figures 8–13 show the space-time dependence of C_2H_6, H_2, C_2H_4, C_2H_2, CH_4, and n-C_4H_{10}, respectively, at three different pressures. It is seen in Fig. 8 that the rate of ethane consumption decreases as pressure is increased. As discussed above, this trend is attributable to a decrease in both the electron

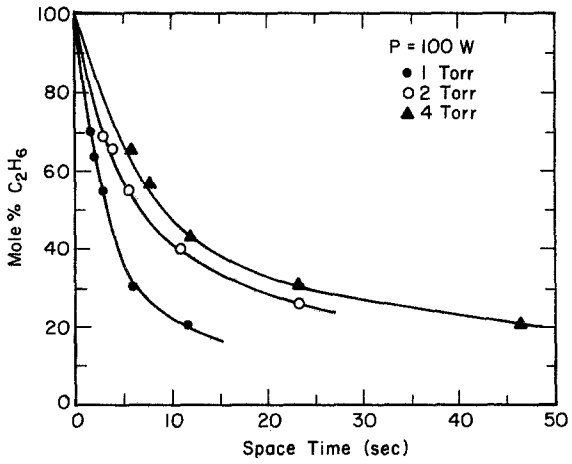

Fig. 8. Effect of pressure on the space-time dependence of C_2H_6 measured in the reactor effluent.

energy and density with increasing pressure, which reduces the rate of monomer dissociation, even though monomer concentration increases. For the same reason, the initial rates of production of H_2, C_2H_4, C_2H_2, and CH_4 decrease with increasing pressure, as seen in Figs. 9–12. The mole percent of H_2 and CH_4 continues to increase out to long space times at all pressures. This indicates that these components are the end products of gas-phase reactions. Ethylene and acetylene, on the other hand, reach a

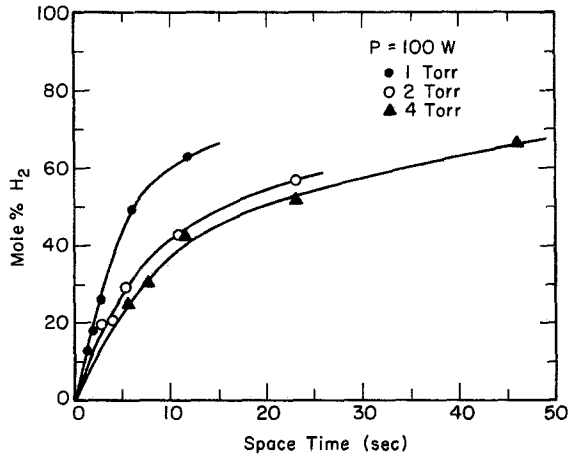

Fig. 9. Effect of pressure on the space-time dependence of H_2 measured in the reactor effluent.

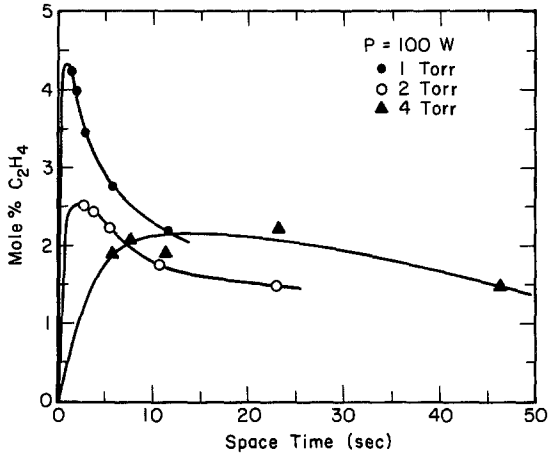

Fig. 10. Effect of pressure on the space-time dependence of C_2H_4 measured in the reactor effluent.

maximum concentration and then decrease with increasing space time. As pressure is increased, this maximum concentration shifts to longer space times. This is due to the slower rate of ethane consumption at higher pressure. The initial rate of production of *n*-butane is relatively independent of pressure, as seen in Fig. 13. However, higher maximum concentrations are reached at higher pressures, due to the factors favoring chain growth

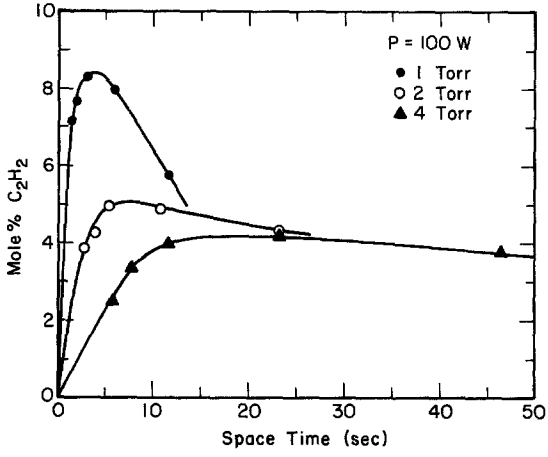

Fig. 11. Effect of pressure on the space-time dependence of C_2H_2 measured in the reactor effluent.

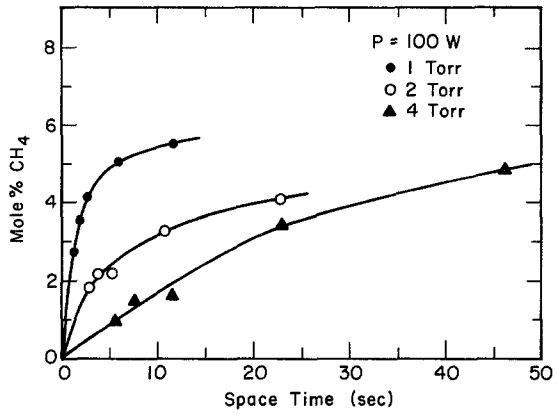

Fig. 12. Effect of pressure on the space-time dependence of CH_4 measured in the reactor effluent.

discussed earlier. The C_3 and C_5 hydrocarbons, and the remaining C_4 products, follow trends very similar to that observed for *n*-butane.

The influence of space-time on the mole fractions of C_2H_6, C_2H_4, C_2H_2, and H_2 at 2 torr and 100 W is plotted together in Fig. 14. It is significant that the concentration of C_2H_4 reaches a maximum at a shorter space time than C_2H_2. This strongly suggests the following sequence of reactions:

$$C_2H_6 \xrightarrow{-H_2} C_2H_4 \xrightarrow{-H_2} C_2H_2$$

The space-time dependences of C_2H_6 and H_2 are also consistent with this

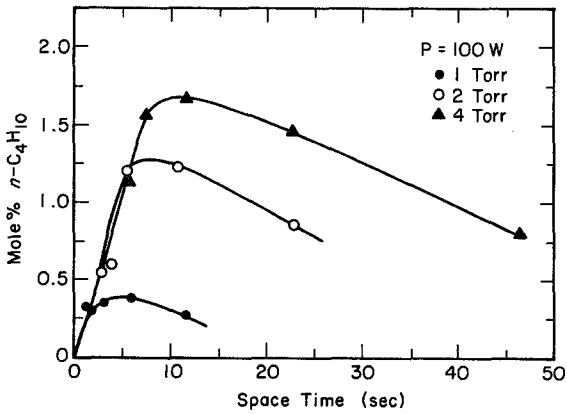

Fig. 13. Effect of pressure on the space-time dependence of n-C_4H_{10} measured in the reactor effluent.

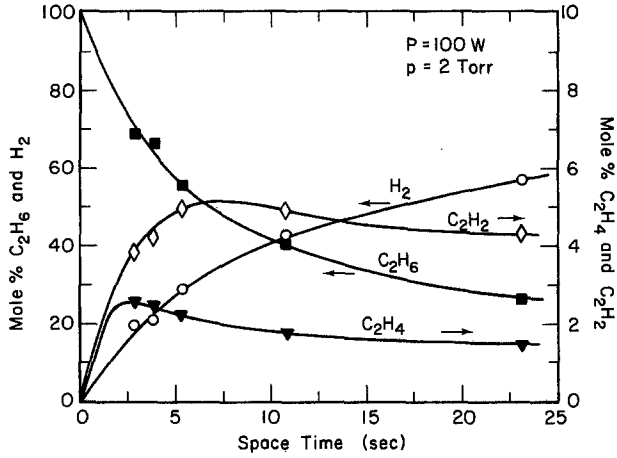

Fig. 14. Space-time dependence of C_2H_6, C_2H_4, C_2H_2, and H_2 in the reactor effluent for a fixed power and pressure.

mechanism. The same trends for these four components were observed at the other pressures.

The effluent analyses discussed above are corroborated by a recent study[27] in which gas-phase products from ethane and methane discharges were analyzed by gas chromatography. Experiments were done in a closed, electrodeless reactor, operating at 13.56 MHz, at pressures of 0.4–1 torr and powers of 25–100 W. Gas-phase composition was analyzed for different discharge times in the closed system. Although none of the reported data were obtained at conditions identical to those used in this study, the distribution breakdown of products is very similar. Also, the dependence of C_2H_6, C_2H_4, C_2H_2, CH_4, and H_2 concentrations on discharge time is similar to the dependence on space time observed in the present work. A general conclusion which can be drawn from this comparison is that the gas-phase reactions occurring in an electrodeless reactor are similar to those occurring in a reactor with parallel-plate electrodes.

3.4. Deposition Rate at a Fixed Position

Figures 15 and 16 show the effects of pressure and power, respectively, on deposition rate as a function of monomer flow rate. These curves resemble similar data obtained for other hydrocarbon monomers.[28,29] At low flow rates, reaction rates are limited by the availability of monomer, and the deposition rate increases as the monomer flow rate increases. At higher flow rates, the residence time available for the formation of reactive

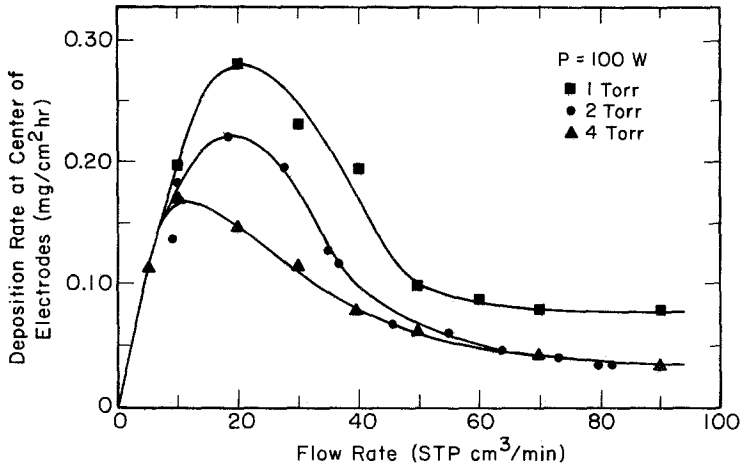

Fig. 15. Effect of pressure on deposition rate at the center of the electrodes as a function of monomer flow rate.

intermediates is reduced, and the deposition rate decreases. The dependence of deposition rate on flow rate is similar to that of ethylene and acetylene. This suggests that film deposition is closely related to the formation of these species in the gas phase.

The effects of pressure and power are more clearly examined by plotting deposition rate as a function of space time. Figure 17 shows that

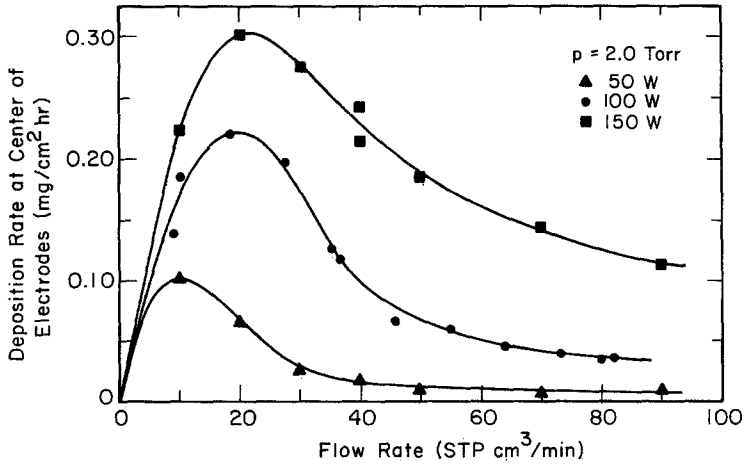

Fig. 16. Effect of power on deposition rate at the center of the electrodes as a function of monomer flow rate.

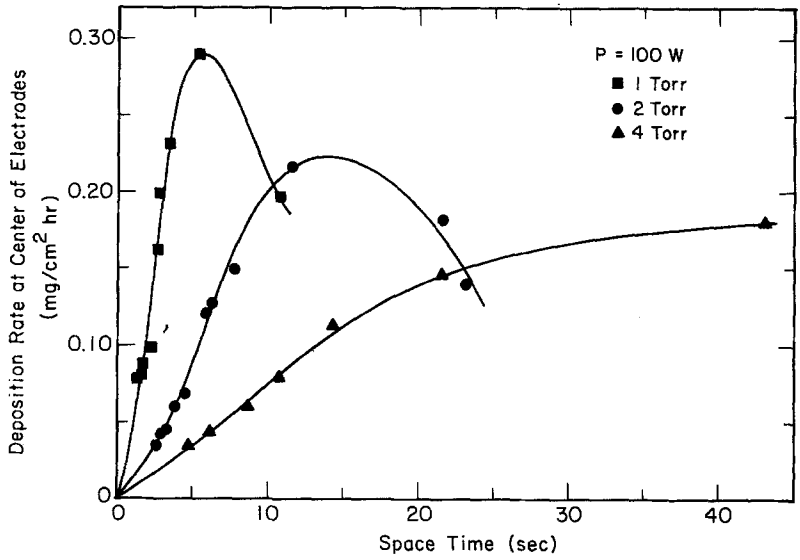

Fig. 17. Effect of pressure on deposition rate at the center of the electrodes as a function of space-time.

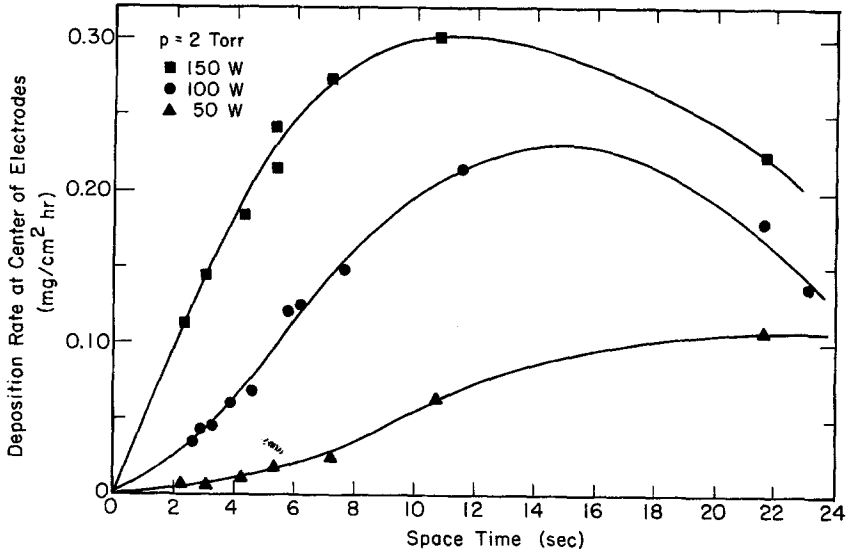

Fig. 18. Effect of power on deposition rate at the center of the electrodes as a function of space-time.

as pressure is increased, the deposition rate increases more slowly with space time, and becomes monomer limited at longer space times. This is similar to the effect of pressure on the space-time dependence of C_2H_4 and C_2H_2, shown in Figs. 10 and 11. A decrease in power has the same qualitative effect as an increase in pressure on deposition rate versus space time, as seen in Fig. 18. Electron density decreases with decreasing power, and electron energy and density both decrease with increasing pressure. Since electron energies and densities determine the rates of electron impact reactions, the data indicate that the dependence of deposition rate on space time is controlled by the rate of electron collisions. An analysis of the relationship between the composition of the gas phase, the rate of polymer deposition, and the experimental variables is the subject of a separate paper[23] and will not be discussed further here.

3.5. Deposition Rate Profiles

Deposition rate profiles were obtained by measuring deposition rates at a number of discrete axial positions both inside and outside the plasma. For reasons discussed previously, it was difficult to obtain deposition rate profiles over a wide range of operating conditions. Pressure, power, and

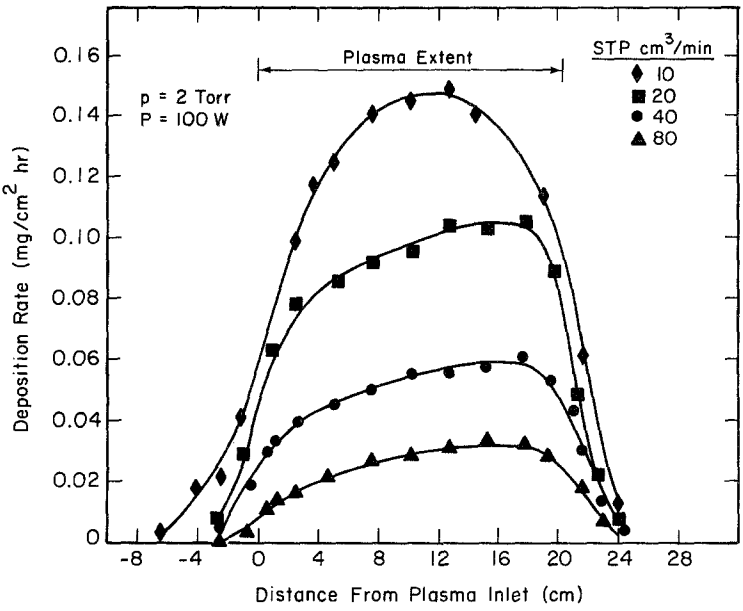

Fig. 19. Effect of monomer flow rate on deposition rate profiles.

monomer flow rate were varied independently, to examine their individual effects on the deposition rate profiles.

The effect of monomer flow rate is shown in Fig. 19. All of the deposition rate profiles are basically bell-shaped curves, flattened in the electrode region and skewed slightly in the direction of flow. Significant deposition occurs outside the plasma region defined by the electrodes, indicating dispersion and convection of the reactive species. Flow rate has a large effect of the magnitude of the curves, but only a moderate effect on their shape, with increased skewing in the direction of flow occurring at higher flow rates. The small change in shape indicates that dispersion effects are dominant over convective effects in determining film thickness distribution.

Figure 20 shows the effect of reaction pressure on the deposition rate profiles. The deposition rate is much greater at 1 torr than at 2 torr: however, it is also slightly greater at 4 torr than at 2 torr. The latter effect may be due to the fact that at 4 torr only a part of the interelectrode space is filled by a visible plasma. Under such circumstances, the power density, and hence the electron density, within the glow becomes greater than if the plasma uniformly filled the interelectrode volume. The profiles become broader as pressure is decreased, due very likely to diffusive transport of polymer precursors both upstream and downstream of the plasma. The

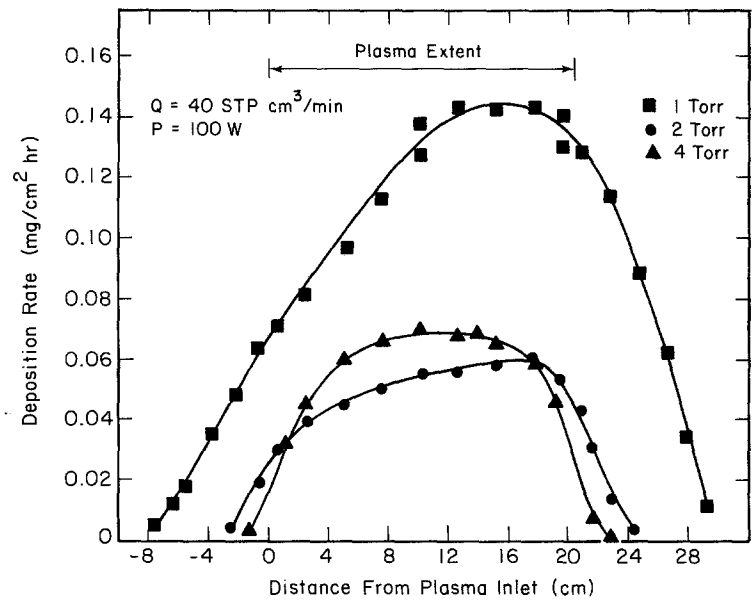

Fig. 20. Effect of pressure on deposition rate profiles.

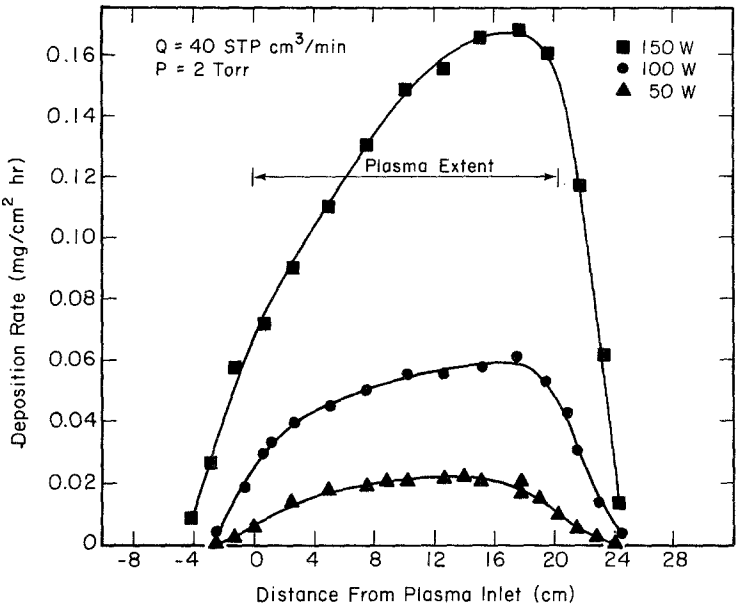

Fig. 21. Effect of power on deposition rate profiles.

very broad profile observed at 1 torr may be due to effects other than diffusion alone. At low pressure, the plasma had the greatest tendency to spread outside the electrode region, especially along the sliding plate and above the sensor head. This probably contributed to artificially high deposition rate measurements outside the plasma.

The effect of discharge power on the deposition rate profiles is shown in Fig. 21. Power has a large effect on the magnitude of the curves. Increasing the power by a factor of three from 50 to 150 W causes a 750% increase in deposition rate at the center of the electrodes. The profiles at lower powers are flatter inside the plasma region, and less skewed in the direction of flow. This effect on the shape of the profiles is similar to that of increased pressure. The profile at 150 W appears broader than the profiles at lower powers, probably due to a spreading of the plasma in a manner similar to that observed at 1 torr.

4. Conclusions

The results of the present study show that the power used to sustain the plasma, the gas pressure, and the monomer space time all have a strong influence on the composition of the gas within the plasma and on the rate and axial uniformity of polymer deposition. Analysis of the effluent gas

composition indicates that C_2H_6 undergoes progressive dehydrogenation to form C_2H_4 and C_2H_2. Since these species are unsaturated, they will be rapidly polymerized, and hence must be regarded as derivative monomers. The cracking of C_2H_6, most likely to form CH_3 and CH_2 radicals, is evidenced by the observation of significant concentrations of CH_4 and other odd-numbered hydrocarbons. While chain propagation to form hydrocarbons containing 3 to 6 carbon atoms is observed, the concentration of these products rapidly declines with increasing carbon number. The effects of the reaction variables on the rate of polymer deposition closely parallel the effects on gas composition, suggesting that the processes responsible for the formation of gaseous products and the deposition of polymer are linked. The measured polymer deposition profiles along the reactor axis show significant nonuniformity within the plasma zone and noticeable polymer depositions in areas immediately upstream and downstream of the plasma. These observations indicate that diffusive and convective transport of derivative monomer and reactive intermediates play an important role in controlling the kinetics of polymer deposition.

REFERENCES

1. V. M. Kolotyrkin, A. B. Gilman, and A. K. Tsapuk, *Russ. Chem. Rev.* **36**, 579 (1967).
2. A. M. Mearns, Thin Solid Films **3**, 201 (1969).
3. A. M. Millard, in *Techniques and Applications of Plasma Chemistry*, J. R. Hollahan and A. T. Bell, eds., Wiley, New York (1974).
4. M. Shen, ed., *Plasma Chemistry of Polymers*, Marcel Dekker, New York (1976).
5. M. R. Havens, M. R. Biolsi, and K. G. Mayhan, *J. Vac. Sci. Technol.* **13**, 575 (1976).
6. H. Yasuda, in *Thin Film Processes*, J. L. Vossen and W. Kern, eds., Academic Press, New York (1978).
7. M. Shen and A. T. Bell, eds., *Plasma Polymerization*, ACS Symp. Ser. 108, Am. Chem. Soc., Washington, D.C. (1979).
8. A. T. Bell, in *Plasma Chemistry III, Topics in Current Chemistry* Vol. 94, S. Vepřek and M. Venugopalan, eds., Springer-Verlag, Berlin, New York (1980).
9. H. Yasuda and C. E. Lamaze, *J. Appl. Polym. Sci.* **17**, 201 (1973).
10. A. T. Bell, T. Wydeven, and C. C. Johnson, *J. Appl. Polym. Sci.* **19**, 1911 (1975).
11. A. F. Stancell and A. T. Spencer, *J. Appl. Polym. Sci.* **16**, 1505 (1972).
12. T. Wydeven and J. R. Hollahan, in *Techniques and Applications of Plasma Chemistry*, J. R. Hollahan and A. T. Bell, eds., Wiley, New York (1974).
13. K. D. Colter, A. T. Bell, and M. Shen, *Biomater., Med. Dev. Artif. Organs* **5**, 1 (1977).
14. K. D. Colter, M. Shen, and A. T. Bell, *Biomater., Med. Dev. Artif. Organs* **5**, 13 (1977).
15. P. J. Ozawa, *IEEE Trans. Parts, Mater. Packag.* **5**, 112 (1969).
16. R. W. Kirk, in *Techniques and Applications of Plasma Chemistry*, J. R. Hollahan and A. T. Bell, eds., Wiley, New York (1974).
17. K. Tien, G. Smolinsky and R. J. Martin, *Appl. Opt.* **11**, 637 (1972).
18. J. R. Hollahan, T. Wydeven, and C. C. Johnson, *Appl. Opt.* **13**, 1844 (1974).
19. T. A. Reis, H. Hirotsuka, A. T. Bell, and M. Shen, *NBS Spec. Publ. Ser* **462**, 230 (1976).

20. K. G. Mayhan, A. W. Hahn, M. R. Havens, and B. W. Peace, *NBS Spec. Publ. Ser.* **415**, 1 (1975).
21. H. Yasuda, M. O. Bumgarner, and N. C. Morosoff, Annual Report on Contract No. NIH-NHLI-73-2913 (1974).
22. J. M. Tibbitt, M. Shen, and A. T. Bell, *J. Macromol. Sci. Chem.* **A10**, 1623 (1976).
23. R. J. Jensen, A. T. Bell, and D. S. Soong, *Plasma Chem. Plasma Proc.* **3**, 163 (1983).
24. H. H. Westberg, R. A. Rasmussen, and M. Holdren, *Annal. Chem.* **46**, 1852 (1974).
25. J. N. Little, W. A. Dark, P. W. Farlinger, and K. J. Bombaugh, *J. Chromatogr. Sci.* **8**, 68 (1967).
26. A. T. Bell, in *Techniques and Applications of Plasma Chemistry*, J. R. Hollahan and A. T. Bell, eds., Wiley, New York (1974).
27. P. Canepa, G. Costello, and M. Nicchia, *Ann. Chim. (Rome)* **68**, 543 (1978).
28. H. Kobasyashi, A. T. Bell, and M. Shen, *Macromolecules* **7**, 277 (1974).
29. J. M. Tibbitt, R. Jensen, A. T. Bell, and M. Shen, *Macromolecules* **10**, 647 (1977).